small methods
www.small-methods.com

Stable $Fe_2P_2S_6$ Nanocrystal Catalyst for High-Efficiency Water Electrolysis

Jinfa Chang, Guanzhi Wang, Anas Belharsa, Junjie Ge, Wei Xing, and Yang Yang**

A crucial step toward clean hydrogen (H_2) energy production through water electrolysis is to develop high-stability catalysts, which can be reliably used at high current densities for a long time. So far, platinum group metals (PGM) and their oxides, for example, Pt and iridium oxide (IrO_2) have been well-regarded as the criterion for hydrogen and oxygen evolution reactions (HER and OER) electrocatalysts. However, the PGM catalysts usually undergo severe performance decay during the long-term operation. Herein, the in situ growth of iron phosphosulfate ($Fe_2P_2S_6$) nanocrystals (NCs) catalysts on carbon paper synthesized by combing chemical vapor deposition with solvent-thermal treatment is reported to show competitive performance and stability as compared to the state-of-the-art PGM catalysts in a real water electrolyzer. A current density of 370 mA cm^{-2} is achieved at 1.8 V when using $Fe_2P_2S_6$ NCs as bifunctional catalysts in an anion exchange membrane water electrolyzer. The $Fe_2P_2S_6$ NCs also show much better stability than the Pt-IrO_2 catalysts at 300 mA cm^{-2} for a continuous 24 h test. The surface generated FeOOH on $Fe_2P_2S_6$ is the real active site for OER. These results indicate that the $Fe_2P_2S_6$ NCs potentially can be used to replace PGM catalysts for practical water electrolyzers.

1. Introduction

The scarcity and overuse of fossil fuels push us to look for sustainable and alternative energy sources, such as hydrogen energy.[1] Different from the conventionally used low-purity hydrogen produced from fossil fuels by reforming processes, the hydrogen obtained by environmentally benign water electrolysis is in high purity for direct utilization without energy-consuming purification treatment. In order to catalyze the bond-breaking and bond-forming reactions involved in the water electrolysis, highly active hydrogen and oxygen evolution reactions (HER) and (OER) catalysts are demanded.[2] Platinum group metals (PGM) and their oxides, such as Pt and IrO_2, have been employed as the benchmark HER and OER catalysts due to their proper surface electronic structures for the reactions.[3] However, in order to keep the current density at a commercially acceptable value, a high cell voltage in a typical range of 1.8–2.0 V is required for the Pt-IrO_2 based water electrolyzer, which is much higher than the standard thermodynamic voltage for water splitting at 1.23 V.[4] In addition, the Pt-IrO_2 based water electrolyzer usually undergoes a serious performance degradation during the long-term operation because of the catalyst deactivation.[5] Hence, it is crucial but still very challenging to develop high-efficiency and high-stability catalysts for realizing the commercialization of water electrolysis technology in large-scale and low energy consumption.

Transition metal phosphosulfides, for example iron phosphosulfides (FeP_xS_y), are emerging catalysts for efficiently catalyzing HER fabricated through mutual replacement between phosphorus (P) and sulfur (S) in the crystalline structure, leading to the tuned electronic structure for the preferred surface adsorption of hydrogen.[6] In addition, the presence of P atoms suppresses the oxidation of Fe and S atoms on the catalyst surface, which is the central importance of stabilizing catalysts in harsh conditions.[7] Thereupon, many $FePS_3$ nanomaterials have been recently developed for electrocatalytic HER and OER.[6e,8] However, the synthesis methods for these $FePS_3$ nanomaterials are very complicated, which are either time-consuming (sometimes 1 week) or energy-consuming (high-temperature and solid-state reactions, more experimental details in Table S1, Supporting Information). Additionally, it is very difficult to completely remove the organic solvent used in these approaches, which may block the active sites and thus reduce the performance of the catalysts. Besides HER, OER is another equally or even more important half-reaction in overall water splitting, which is always the performance-determining process because of its sluggish four-electron transfer kinetics. The rational design of OER and HER catalysts that both work efficiently in the same electrolyte and operation conditions in the water electrolyzer is urgently needed. While recent research

Dr. J. Chang, G. Wang, A. Belharsa, Prof. Y. Yang
NanoScience Technology Center
Department of Materials Science and Engineering
Energy Conversion and Propulsion Cluster
University of Central Florida
12424 Research Parkway, Suite 423, Orlando, FL 32826, USA
E-mail: Yang.Yang@ucf.edu
Prof. J. Ge, Prof. W. Xing
State Key Laboratory of Electroanalytical Chemistry
Laboratory of Advanced Power Sources
Jilin Province Key Laboratory of Low Carbon Chemical Power Sources
Changchun Institute of Applied Chemistry
5625 Renmin Street, Changchun 130022, P. R. China
E-mail: gejj@ciac.ac.cn
The ORCID identification number(s) for the author(s) of this article can be found under https://doi.org/10.1002/smtd.201900632.

DOI: 10.1002/smtd.201900632

indicates that the surface oxidization and the transition metal oxides, hydroxides, high valence oxyhydroxides formed on the materials surfaces are the real active phase for OER. [8a,9] Therefore, many bifunctional catalysts have been developed in the three-electrode electrochemical cells.[10] Using the bifunctional catalysts in a real water electrolyzer will simplify the water electrolyzer cell structure and improve the overall device efficiency, however, which is still very challenging.[11]

Herein, we report a facial method to synthesize $Fe_2P_2S_6$ NCs on conductive carbon papers using a solvent-thermal reaction followed by chemical vapor deposition (CVD) treatment. The as-prepared $Fe_2P_2S_6$ NCs were directly used as bifunctional HER/OER catalysts in a strong base solution. In a three-electrode electrochemical cell, the $Fe_2P_2S_6$ NCs require only 0.33 and 0.39 V to reach 100 mA cm^{-2} for HER and OER, respectively, which are much better than the benchmark IrO_2 catalyst. The detailed study indicates that $Fe_2P_2S_6$ NCs are responsible for HER, while the surface FeOOH on $Fe_2P_2S_6$ NCs is the real active phase for OER. In a practical anion exchange membrane water electrolyzer, the bifunctional $Fe_2P_2S_6$ NCs deliver an outstanding current density of 370 mA cm^{-2} at 1.8 V, which is very close to the state-of-the-art Pt-IrO_2 catalysts. More important, the $Fe_2P_2S_6$ NCs show considerably better stability than the Pt-IrO_2 catalyst when tested at 300 mA cm^{-2} continuously for 24 h. This work provides a new route for the rational design of robust catalysts for practical water splitting applications.

2. Results and Discussion

The in situ synthesis of $Fe_2P_2S_6$ NCs on carbon paper is schematically illustrated in **Scheme 1**. More specifically, $Fe(NO_3)_3 \cdot 9H_2O$, NH_4F, and $(NH_2)_2CO$ were dissolved in deionized water under ultrasonic and then transferred to polytetrafluoroethylene (PTFE)-lined stainless steel autoclave containing the precleaned carbon paper at 120 °C for 5 h. After solvent-thermal treatment, the carbon paper was fully covered by FeO(OH) NCs (Figure S1, Supporting Information). Afterward, the FeO(OH) NCs were placed in the CVD tube furnace at the downstream end of the tube and a certain amount of sulfur powders and $NaH_2PO_2 \cdot H_2O$ mixture at the mole ratio of 1:3 was placed at the upstream of the tube. The furnace was then heated to 300 °C for 1 h with the ramping rate of 2 °C min^{-1} in order to convert the FeO(OH) NCs precursors to the $Fe_2P_2S_6$ NCs.

The crystalline structures of the $Fe_2P_2S_6$ NCs were studied by X-ray diffraction (XRD, **Figure 1**a), which shows the well-indexed $(20\bar{1})$, $(13\bar{1})$, $(20\bar{2})$, $(13\bar{2})$, $(13\bar{3})$, (331), $(20\bar{4})$, and $(26\bar{1})$ planes of monoclinic $Fe_2P_2S_6$ phase (JCPDS No. 33-0672). The morphology of the $Fe_2P_2S_6$ NCs was examined by scanning electron microscopy (SEM, Figure 1b), which clearly shows complete coverage of carbon paper by the $Fe_2P_2S_6$ NCs. Transmission electron microscopy (TEM, Figure 1c) image indicates that the average particle size of the $Fe_2P_2S_6$ NCs is about 13.8 mm (Figure S2, Supporting Information). The high-resolution TEM image (Figure 1d) clearly shows the interplanar distance of 2.54 Á, which is indexed to the $(20\bar{2})$ plane of $Fe_2P_2S_6$. The selected area electron diffraction (SAED, Figure 1e) pattern shows discrete spots/circular rings, which are indexed to the $(20\bar{2})$, $(26\bar{1})$, and $(13\bar{2})$ planes of $Fe_2P_2S_6$. The high-angle annular dark-field (HAADF) scanning transmission electron microscopy coupled with energy-dispersive X-ray spectroscopy elemental mapping images (Figure 1f) shows the uniform distribution of Fe, P, and S elements throughout the entire materials. The contents of Fe, P, and S are estimated to be 30.1, 16.9, and 52.9 wt%, respectively, detected by inductively coupled plasma-atomic emission spectrometry, further confirming the successful synthesis of the $Fe_2P_2S_6$ NCs.

The FeP NCs (Figure S3, Supporting Information) and FeS_2 NCs (Figure S4, Supporting Information) were synthesized as control samples using the same method. The X-ray photoelectron spectroscopy (XPS) Fe 2p profiles (**Figure 2**a) for the $Fe_2P_2S_6$ NCs, FeP NCs, and FeS_2 NCs show that the peaks centered at 711 and 724 eV are attributed to Fe $2p_{3/2}$ and $2p_{1/2}$, respectively, indicating the presence of Fe^{3+} along with Fe^{2+} in the $Fe_2P_2S_6$ NCs. The peaks located at 714.5 and 727.5 eV are assigned to Fe $2p_{3/2}$ and $2p_{1/2}$ of Fe^{3+}. The peak at 719 eV is the satellite peak of Fe 2p. For the $Fe_2P_2S_6$ NCs, a small peak at 706.7 eV is ascribed to Fe $2p_{3/2}$ for metallic Fe, which is consistent with other transition metal (Co, Ni, Mo) phosphosulfides with restrained surface oxidation of the materials.[6a,c,12] The coexistence of Fe^{3+} and Fe^{2+} in the materials plays a key role in improving the electronic conductivity.[6e] The XPS P 2p profiles for in FeP NCs (Figure 2b) show only one peak at 134.0 eV, which is attributed to P-O in the FeP NCs. Whereas, the $Fe_2P_2S_6$ NCs show two XPS peaks that can be assigned to the phosphide at 129.3 eV and P-O at 133.3 eV.[13] The XPS S 2p profile (Figure 2c) for the $Fe_2P_2S_6$ NCs shows a dominant peak at 163.7 eV and a minor peak at 168.8 eV, corresponding to the characteristic peaks of sulfide and S-O, respectively.[6c] While for the FeS_2 NCs, a dominated peak at 168.9 eV and a small peak at 164.0 eV were observed. The surface oxidation is a common phenomenon for the transition metal-based materials when exposing to the air.[14] Some

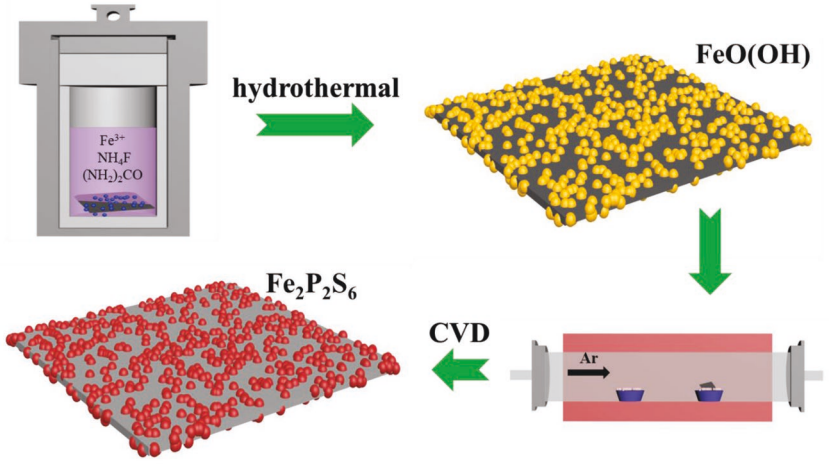

Scheme 1. Schematic illustration for the in situ synthesis of the $Fe_2P_2S_6$ NCs on carbon paper.

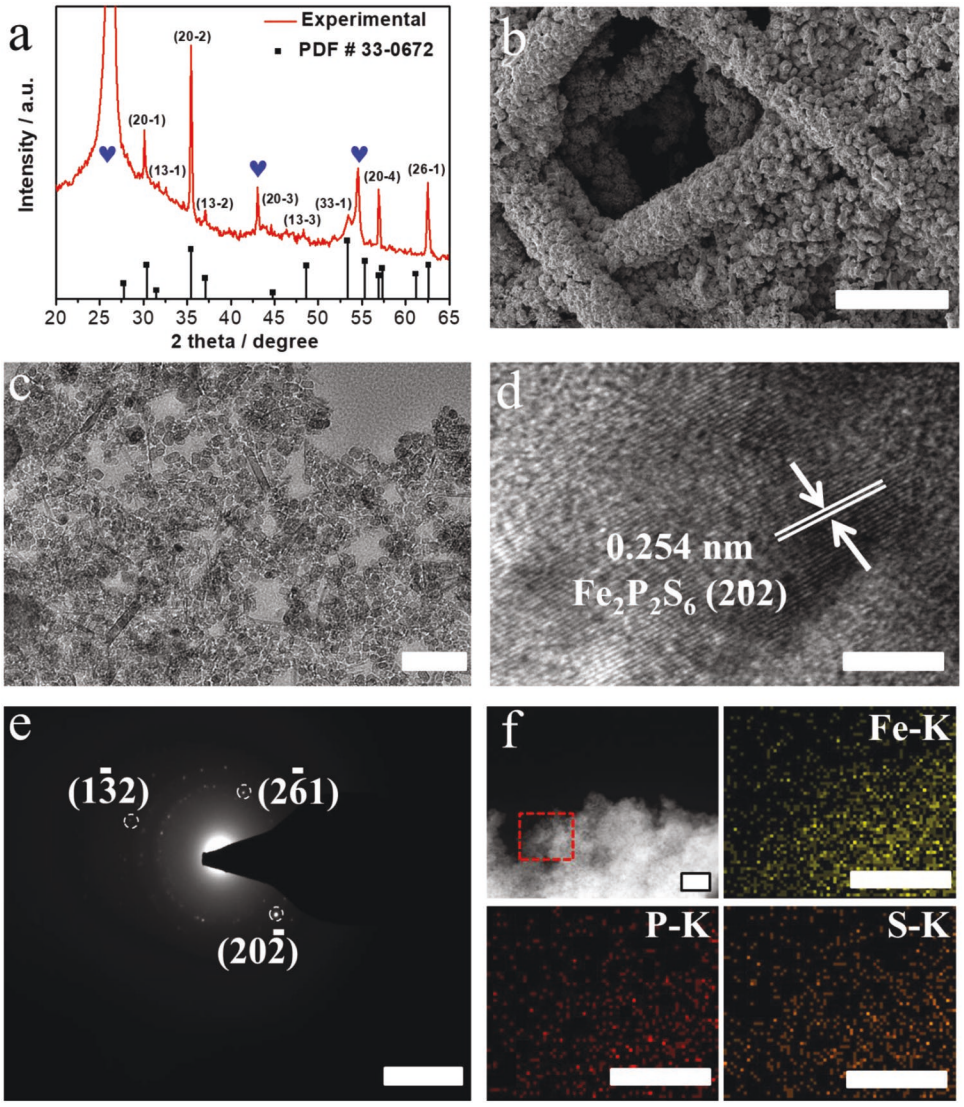

Figure 1. a) XRD patterns, the peaks of carbon paper are marked as "♥." b) SEM. c) TEM. d) HR-TEM. e) SAED. f) HAADF and elemental mapping images of the $Fe_2P_2S_6$ NCs. The elemental mapping images were taken from the red-dotted region marked in (f). Scale bars denote b) 50 µm, c) 100 nm, d) 5 nm, e) 5 1/nm, and f) 200 nm.

attempts to reduce the surface oxide by heat treatment at high temperature under argon has been demonstrated to be unsuccessful.[15] These XPS results further indicate that the surface oxidation of the $Fe_2P_2S_6$ NCs is significantly suppressed due to the mutual replacement between P and S, thus leading to a robust and stabilized electrocatalytic performance.[12b] In addition, due to the strong electronic interactions between Fe and PS_3 subunits,[6a,e] the Fe 2p in $Fe_2P_2S_6$ have a positive shift toward the higher binding energy, meanwhile, the P 2p and S 2p in $Fe_2P_2S_6$ have a negative shift toward the lower binding energy as compare to those in FeP and FeS_2.

The catalytic HER activity of the $Fe_2P_2S_6$ NCs was conducted in the Ar-saturated 1 M KOH electrolyte. The performance of the FeP NCs, FeS_2 NCs, commercial Pt/C, and carbon paper was also tested as a comparison. As shown in **Figure 3**a, the bare carbon paper has no HER catalytic activity. While a rapid increase in the cathodic current was observed for all the other samples. The overpotentials for the $Fe_2P_2S_6$ NCs, FeP NCs, FeS_2 NCs, and Pt/C are 0.175, 0.236, 0.310, and 0.090 V, respectively, to reach the current density of 10 mA cm^{-2}. At the overpotential of 0.33 V, the $Fe_2P_2S_6$ NCs show a current density of 100 mA cm^{-2}, much higher than the Pt/C catalyst (43.7 mA cm^{-2}). The much better performance of the $Fe_2P_2S_6$ NCs than the Pt/C at higher current densities is beneficial for an actual water electrolyzer operated at high current density. The Tafel slopes (Figure 3b) are calculated to be 137, 217, 231, and 62 mV dec^{-1} for the $Fe_2P_2S_6$ NCs, FeP NCs, FeS_2 NCs, and Pt/C, respectively. The Tafel slope for the $Fe_2P_2S_6$ NCs is much smaller than the FeP NCs and FeS_2 NCs, indicating the facilitated HER kinetics for the $Fe_2P_2S_6$ NCs. The $Fe_2P_2S_6$ NCs also show much better HER performance than the state-of-the-art MPS_3 (M = Fe, Ni, Co, and Bi; for the complete list please see Table S2, Supporting Information). Furthermore, the OER activity was tested in the O_2-saturated 1 M KOH

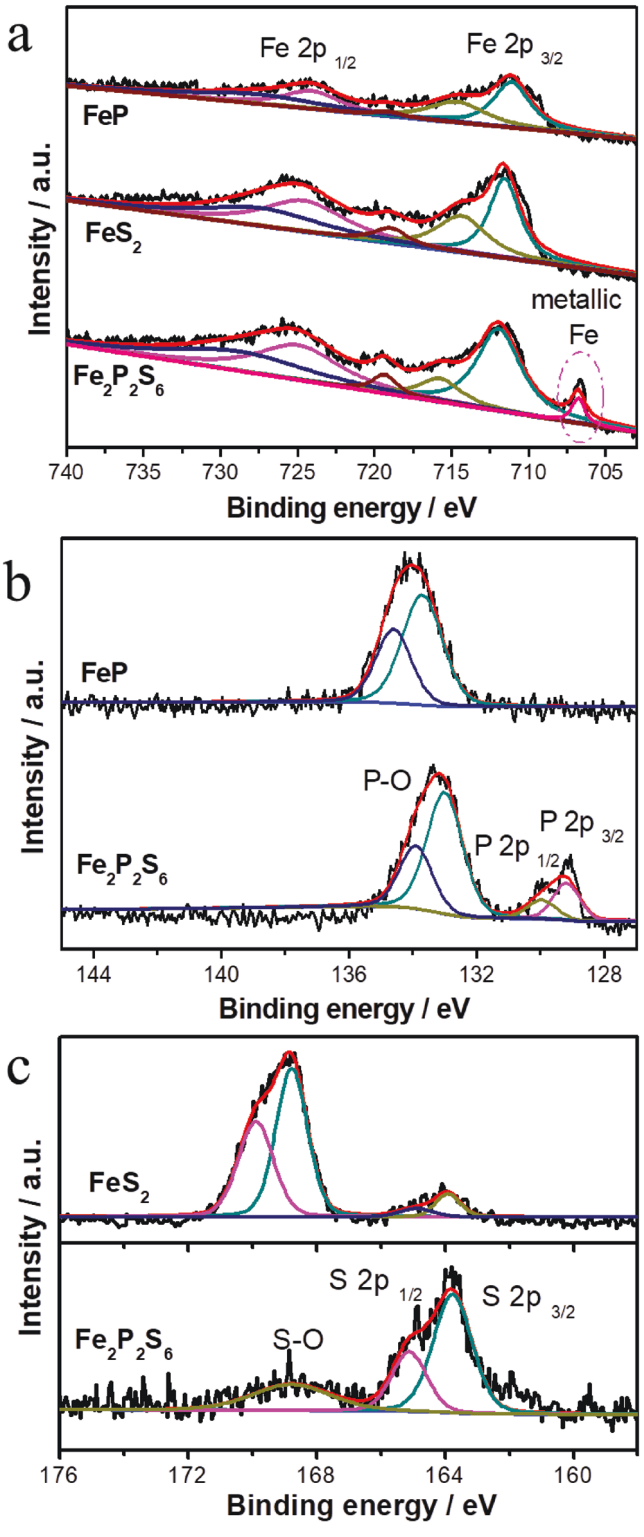

Figure 2. a–c) XPS Fe 2p, P 2p, and S 2p spectra for the $Fe_2P_2S_6$ NCs, FeP NCs, and FeS_2 NCs, respectively.

solution. The Linear sweep voltammetric (LSV) curves for the $Fe_2P_2S_6$ NCs (Figure 3c) shows decreased overpotentials of 0.288, 0.309, and 0.395 V to reach the current densities at 10, 20, and 100 mA cm^{-2}, respectively, much better than that of IrO_2 (overpotentials of 0.321 and 0.349 V to reach current densities of 10 and 20 mA cm^{-2}). As control samples, the FeP NCs and FeS_2 NCs show inferior performance than that of the $Fe_2P_2S_6$ NCs, which need much higher overpotentials to reach the same current densities. Moreover, the Tafel slope for the $Fe_2P_2S_6$ NCs (Figure 3d, 45.7 mV dec^{-1}) is much lower than the FeP NCs (65.1 mV dec^{-1}), FeS_2 NCs (58.1 mV dec^{-1}), IrO_2 (59.3 mV dec^{-1}), and other $FePS_3$ nanomaterials (58.1 mV dec^{-1}, Table S2, Supporting Information),[8a,9c] indicating the favorable OER kinetics for the $Fe_2P_2S_6$ NCs. In addition, the HER and OER activities were further normalized to electrochemically active surface area (ECSA) (Figure S5, Supporting Information). It is clear that the $Fe_2P_2S_6$ still possesses the best performance for both HER and OER as compared to FeP and FeS_2, thus indicating the impressive intrinsic activity of $Fe_2P_2S_6$ (or the derivate species) for HER and OER.

Electrochemical impedance spectroscopy was further adopted to study electrode reaction kinetics of the materials. The Nyquist plots for the $Fe_2P_2S_6$ NCs, FeP NCs, and FeS_2 NCs were tested at an overpotential of 0.2 V for HER (Figure S6a, Supporting Information) and 0.32 V for OER (Figure S6b, Supporting Information) in 1 M KOH. The $Fe_2P_2S_6$ NCs exhibits the smallest charge transfer resistance (R_{CT}), indicating the fastest electrode kinetics as compared to other control samples. The electrochemical double-layer capacitances (C_{dl}, Figure S7, Supporting Information) show a proportional relationship to the electrochemical surface areas. The C_{dl} of the $Fe_2P_2S_6$ NCs is as high as 15.3 mF cm^{-2}, which is much higher than that of the FeP NCs (8.1 mF cm^{-2}) and FeS_2 NCs (3.0 mF cm^{-2}), indicating much higher surface roughness and more catalytically available active sites of the $Fe_2P_2S_6$ NCs. The long-term stability tests (Figure S8, Supporting Information) of the $Fe_2P_2S_6$ NCs for HER and OER were conducted by chronoamperometry at overpotentials of 0.2 and 0.32 V, respectively, further confirming the excellent electrochemical stability of the catalyst. The attenuation of OER performance should be mainly caused by the bubble blockage of the active surface during the OER.[16]

Inspired by the impressive HER and OER activities in the base solution, the $Fe_2P_2S_6$ NCs were further used as bifunctional catalysts in a real electrolyzer as both anode and cathode with anion exchange membrane as the solid electrolyte (**Figure 4**a, and Figure S9, Supporting Information). At 50 °C, the electrolyzer delivers an output current density of 370 mA cm^{-2} at 1.8 V (Figure 4b), which is very close to the conventional electrolyzer using the Pt/IrO_2 catalysts (400 mA cm^{-2} at 1.8 V). Figure 4c shows the *V*–*t* curves of the electrolyzer at a constant current density of 300 mA cm^{-2}. The cell voltage increases from 1.70 to 1.84 V by 0.14 V in the cell using the Pt/IrO_2 catalyst after 24 h stability test. While the cell voltage only increases by 0.02 V (from 1.74 to 1.76 V) in the cell using the $Fe_2P_2S_6$ NCs bifunctional catalysts, indicating the supreme stability of the materials. In order to probe the potential commercial application, the performance of water electrolyzer using the $Fe_2P_2S_6$ NCs as bifunctional catalysts at ambient temperature and pressure was tested (Figure S10a, Supporting Information), which deliver a current density of 154 mA cm^{-2} at 1.8 V. The long-time stability at the current density of 10 and 100 mA cm^{-2} was shown in Figure S10b (Supporting Information). After 24 h of long-time

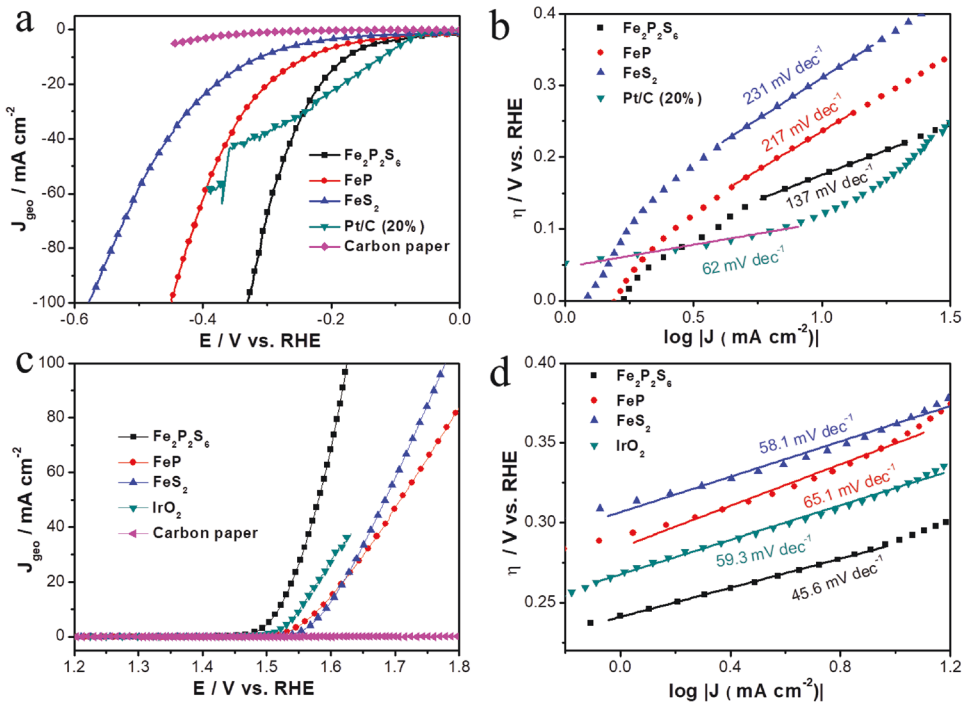

Figure 3. a) Linear sweep voltammetric (LSV) curves for HER and b) the corresponding Tafel slopes of the $Fe_2P_2S_6$ NCs, FeP NCs, FeS_2 NCs, commercial Pt/C, and bare carbon paper in Ar-saturated 1 M KOH (scan rate: 5 mV s^{-1}, 90% iR-corrected). c) LSV curves for OER and d) the corresponding Tafel slopes of the $Fe_2P_2S_6$ NCs, FeP NCs, FeS_2 NCs, commercial IrO_2, and bare carbon paper in O_2-saturated 1 M KOH (scan rate: 5 mV s^{-1}, 90% iR-corrected). Catalyst loading of 0.2 mg cm^{-2} for all sampes. The current density was normalized to the geometry area of the electrode.

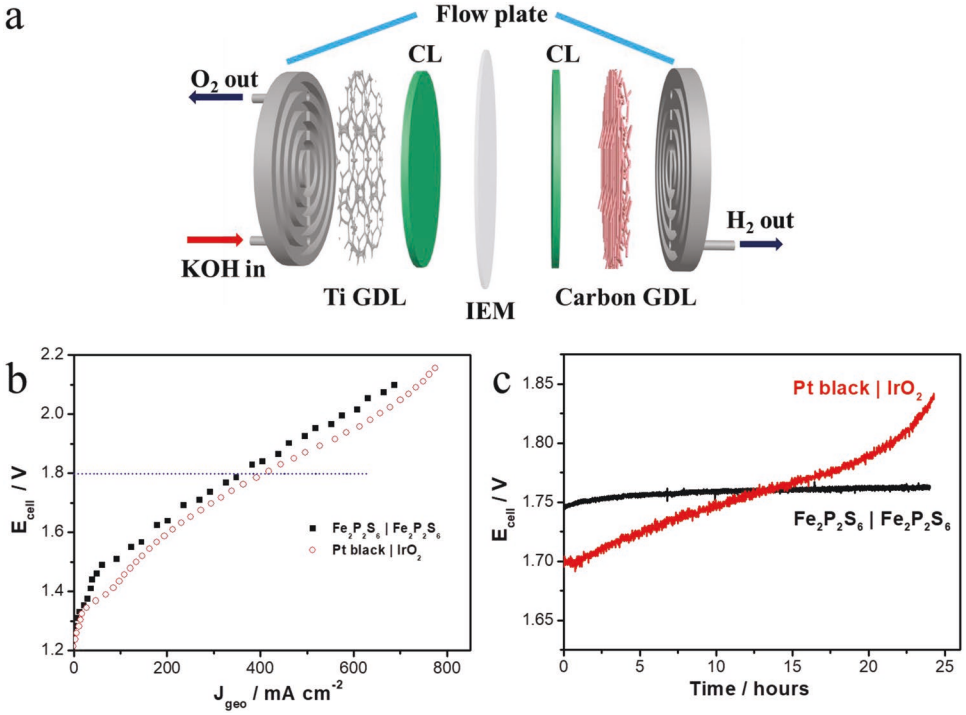

Figure 4. a) Schematic illustration of the actual water electrolyzer used in this work. GDL: gas diffusion layer; CL: catalyst layer; IEM: ion exchange membrane. b) LSV polarization curves and c) the corresponding *V*–*t* curves at a current density of 300 mA cm^{-2}. The catalyst loading was 2 mg cm^{-2} on both electrodes. 1 M KOH was feed into the anode side at a flow rate of 5 mL min^{-1}. Test temperature: 50 °C at the ambient pressure.

stability test, the voltage increases by only 6 and 12 mV, respectively, indicating the excellent stability of $Fe_2P_2S_6$ NCs for practical water electrolysis. It should be noted that the stability of the real water electrolyzer is much better than that tested in the three-electrode half cell. That is because the gas bubbles occupy the active site thus result in the performance degradation in the three-electrode test without forced convection. While in the real water electrolyzer, the KOH solution was supplied into the anode chamber with a liquid pump, removing the gas bubbles. This result aligns with recent reports, proving the OER activity degradation caused by the bubble blockage of the active surface in the three-electrode electrochemical systems.[16]

Previous studies indicated that bulk $FePS_3$ is a semiconductor, which is not ideal for electrochemical reaction.[9b] Some strategies, such as exfoliating ultrathin $FePS_3$ layers,[8a,9a] doping by other metal,[9c,17] and coupling with conductive reduced graphene oxide[6e] have been adopted to improve the HER and OER activities. In this work, the greatly improved HER and OER activities are attributed to the in situ growth of $Fe_2P_2S_6$ NCs on carbon paper. To confirm this conclusion, the $Fe_2P_2S_6$ NCs without carbon paper was synthesized and was dropped (Nafion as the binder) on glassy carbon electrode and carbon paper electrode, respectively. As a result, worse HER and OER performance (Figure S11, Supporting Information) were obtained for both control experiments as compared to the in situ growth of $Fe_2P_2S_6$ NCs on carbon paper at the same loading. These control experiments prove that the in situ growth of $Fe_2P_2S_6$ on carbon paper is the main reason for the improved electrochemical performance, consistent with the previous reports.[6e] These binder-free and uniformly dispersed $Fe_2P_2S_6$ NCs with abundant active sites on the carbon paper avoid catalyst aggregation. Moreover, the in situ growth of $Fe_2P_2S_6$ NCs on carbon paper ensures the good interaction between carbon paper and $Fe_2P_2S_6$ NCs, which results in high electrical conductivity and low electron transfer resistance, and further facilitate the charge transfer.

After the long-term stability test, the catalysts at both the anode side and cathode side were characterized by XRD and XPS. The XRD patterns (Figure S12, Supporting Information) show no distinguishable change in the bulk crystalline structure, indicating the ultrahigh stability of the $Fe_2P_2S_6$ NCs. The XPS Fe 2p profiles of the $Fe_2P_2S_6$ NCs (Figure S13, Supporting Information) before and after stability tests show almost no change, except for the disappearance of the metallic Fe due to the surface reconstruction of the catalyst during water oxidation reaction in a strongly alkaline solution. The surface reconstruction was also observed in the decreased XPS P 2p (Figure S14, Supporting Information) and S 2p (Figure S15, Supporting Information) peaks intensities, which have been also reported by other OER catalysts tested in alkaline solution. The high-resolution O 1s XPS after the OER test was deconvoluted to probe the real active site of $Fe_2P_2S_6$ NCs (Figure S16, Supporting Information). Two peaks centered at 528.4 and 529.9 eV are associated with Fe—O—Fe and Fe—O—H bonds in FeOOH, respectively.[18] The peak located at 531.7 eV is the characteristic signal of oxygen in the surface adsorbed water. The XPS results indicate that the FeOOH as a main active phase is formed on the surface of $Fe_2P_2S_6$ during OER. The O 1s XPS of $Fe_2P_2S_6$ NCs, FeP NCs, and FeS_2 NCs after HER and OER were further compared in Figure S17 (Supporting Information). After HER, two peaks located at 530.8 and 531.7 eV were observed, which can be assigned to oxygen in —OH groups and surface adsorbed water, respectively. While for all samples after the OER tests, a peak located at 528.4 eV is attributed to the Fe—O—Fe bonds in FeOOH,[18] which is consistent with previous reports.[9c,19] Table S4 (Supporting Information) shows the elemental contents of the as-prepared sample and the sample after the OER test examined by energy dispersive spectrometer (EDS). Oxygen exists in the freshly prepared samples due to the natural surface oxidation when exposing to the air. The O content in $Fe_2P_2S_6$ NCs is much lower than that in FeP NCs and FeS_2 NCs. While after OER, the O content of all samples increases due to the surface oxidation in strongly alkaline conditions.[14] Furthermore, the Raman spectrum (Figure S18, Supporting Information) shows that after the OER test, new characteristic Raman peaks at 298 and 394 cm^{-1} attributed to FeOOH are observed in addition to the characteristic Raman peaks of $Fe_2P_2S_6$ (129, 176, 254, 383, and 588 cm^{-1}).[20] The Raman results further confirm the formation of iron oxides/hydroxides on the surface of $Fe_2P_2S_6$. The XPS, EDS, and Raman results indicate that the FeOOH formed on the surface of $Fe_2P_2S_6$ NCs should be the main active site/phase for OER.

To further verify if the oxidized Fe species are the catalytic active phase for HER and OER (Figure S19a, Supporting Information), the FeOOH and Fe_2O_3 in situ grown on carbon papers were further studied.[21] Except for the double-layer capacitive current, the FeOOH and Fe_2O_3 show no obvious catalytic activity for HER before −0.5 and −0.4 V, respectively. The insufficient HER activity of these oxidized Fe species has a negligible contribution to the excellent HER activity of $Fe_2P_2S_6$. Thereupon, the possibility of oxidized Fe species being the active sites in $Fe_2P_2S_6$ for HER can be ruled out. While both FeOOH and Fe_2O_3 possess considerable OER activities (Figure S19b, Supporting Information) at an overpotential of 0.35 V to produce a current density of 10 mA cm^{-2}. These results are consistent with XRD, XPS, and Raman investigations, further confirming that the oxidized Fe species (especially FeOOH) on the surface of $Fe_2P_2S_6$ is the catalytic active phase for OER.

It has been well-accepted that the transition metal phosphosulfides show worse stability in acid solution than in alkaline solution. Thus, we further test the catalytic performance of all samples in 0.5 M H_2SO_4 solution (Figure S20, Supporting Information). The $Fe_2P_2S_6$ NCs show low overpotentials of 0.043 and 0.143 V to reach current densities of 10 and 100 mA cm^{-2}. The Tafel slope for the $Fe_2P_2S_6$ NCs is only 71.2 mV dec^{-1}, much lower than that of the FeP NCs (97.3 mV dec^{-1}), FeS_2 NCs (85.1 mV dec^{-1}), and other $FePS_3$ nanomaterials (Table S2, Supporting Information). In addition, after the 5000 cycles accelerated aging test (Figure S21, Supporting Information), the $Fe_2P_2S_6$ NCs show the minimal performance decay as compared to the FeP NCs and FeS_2 NCs, confirming the excellent stability in acid solution.

3. Conclusions

In summary, we have demonstrated that the $Fe_2P_2S_6$ NCs synthesized by combing solvent-thermal with CVD are highly efficient and stable electrocatalysts in both alkaline and acid media, the oxidized Fe species (FeOOH) on the surface of

$Fe_2P_2S_6$ is the real catalytic active phase for OER. The current density of 370 mA cm^{-2} was achieved at 1.8 V in a real water electrolyzer using the $Fe_2P_2S_6$ NCs as bifunctional catalysts for both anode and cathode, delivering superior stability to the Pt/IrO_2 catalysts. The proposed method will promote the commercialization of PGM-free catalysts with mass production in actual energy devices.

4. Experimental Section

For experimental details, see the Supporting Information.

Supporting Information

Supporting Information is available from the Wiley Online Library or from the author.

Acknowledgements

Y.Y. acknowledges the financial support from the National Science Foundation under Grant No. CMMI-1851674, the National Aeronautics and Space Administration (NASA) through the University of Central Florida's NASA Florida Space Grant Consortium and Space Florida, and the startup support (20080741) from the University of Central Florida. J.C. acknowledges the financial support from the Preeminent Postdoctoral Program (P3) at the University of Central Florida. The XPS test was supported by the NSF MRI: XPS: ECCS: 1726636, hosted in MCF-AMPAC facility, MSE, CECS, UCF. W.X. and J.G. acknowledges the National Major Science and Technology Projects of China (No. 2017YFB0102900), the National Natural Science Foundation of China (Nos. 21633008, 21433003, 21733004, and U1601211), Jilin Scientific and Technological Development Program (Nos. 20150101066JC, 20160622037JC, 20170203003SF, and 20170520150JH), the Recruitment Program of Foreign Experts (No. WQ20122200077) and the Hundred Talents Program of Chinese Academy of Sciences. The authors thank Prof. Nina Orlovskaya and Ruslan Kuliiev for Raman measurements.

Conflict of Interest

The authors declare no conflict of interest.

Keywords

bifunctional catalysts, iron phosphosulfide, nanocrystals, stability, water electrolysis

Received: September 12, 2019
Revised: October 20, 2019
Published online:

[1] a) P. De Luna, C. Hahn, D. Higgins, S. A. Jaffer, T. F. Jaramillo, E. H. Sargent, *Science* **2019**, *364*, eaav3506; b) X. Zou, Y. Zhang, *Chem. Soc. Rev.* **2015**, *44*, 5148; c) Y. Hou, X. Zhuang, X. Feng, *Small Methods* **2017**, *1*, 1700090.

[2] a) H. Shi, H. Liang, F. Ming, Z. Wang, *Angew. Chem., Int. Ed.* **2017**, *56*, 573; b) Y. Shi, B. Zhang, *Chem. Soc. Rev.* **2016**, *45*, 1529; c) H. Duan, D. Li, Y. Tang, Y. He, S. Ji, R. Wang, H. Lv, P. P. Lopes, A. P. Paulikas, H. Li, S. X. Mao, C. Wang, N. M. Markovic, J. Li, V. R. Stamenkovic, Y. Li, *J. Am. Chem. Soc.* **2017**, *139*, 5494.

[3] a) J. Wang, F. Xu, H. Jin, Y. Chen, Y. Wang, *Adv. Mater.* **2017**, *29*, 1605838; b) Y. Xu, W. Tu, B. Zhang, S. Yin, Y. Huang, M. Kraft, R. Xu, *Adv. Mater.* **2017**, *29*, 1605957; c) M. Sun, H. Liu, J. Qu, J. Li, *Adv. Energy Mater.* **2016**, *6*, 1600087; d) J. Li, Y. Wang, T. Zhou, H. Zhang, X. Sun, J. Tang, L. Zhang, A. M. Al-Enizi, Z. Yang, G. Zheng, *J. Am. Chem. Soc.* **2015**, *137*, 14305.

[4] C. G. Morales-Guio, L. A. Stern, X. Hu, *Chem. Soc. Rev.* **2014**, *43*, 6555.

[5] F. Luo, Q. Zhang, X. Yu, S. Xiao, Y. Ling, H. Hu, L. Guo, Z. Yang, L. Huang, W. Cai, H. Cheng, *Angew. Chem., Int. Ed.* **2018**, *57*, 14862.

[6] a) M. Caban-Acevedo, M. L. Stone, J. R. Schmidt, J. G. Thomas, Q. Ding, H. C. Chang, M. L. Tsai, J. H. He, S. Jin, *Nat. Mater.* **2015**, *14*, 1245; b) K. Liang, S. Pakhira, Z. Yang, A. Nijamudheen, L. Ju, M. Wang, C. I. Aguirre-Velez, G. E. Sterbinsky, Y. Du, Z. Feng, J. L. Mendoza-Cortes, Y. Yang, *ACS Catal.* **2019**, *9*, 651; c) J. Chang, K. Li, Z. Wu, J. Ge, C. Liu, W. Xing, *ACS Appl. Mater. Interfaces* **2018**, *10*, 26303; d) W. Liu, E. Hu, H. Jiang, Y. Xiang, Z. Weng, M. Li, Q. Fan, X. Yu, E. I. Altman, H. Wang, *Nat. Commun.* **2016**, *7*, 10771; e) D. Mukherjee, P. M. Austeria, S. Sampath, *ACS Energy Lett.* **2016**, *1*, 367.

[7] Z. Wu, X. Li, W. Liu, Y. Zhong, Q. Gan, X. Li, H. Wang, *ACS Catal.* **2017**, *7*, 4026.

[8] a) W. Zhu, W. Gan, Z. Muhammad, C. Wang, C. Wu, H. Liu, D. Liu, K. Zhang, Q. He, H. Jiang, X. Zheng, Z. Sun, S. Chen, L. Song, *Chem. Commun.* **2018**, *54*, 4481; b) Z. Yu, J. Peng, Y. Liu, W. Liu, H. Liu, Y. Guo, *J. Mater. Chem. A* **2019**, *7*, 13928.

[9] a) R. Dangol, Z. Dai, A. Chaturvedi, Y. Zheng, Y. Zhang, K. N. Dinh, B. Li, Y. Zong, Q. Yan, *Nanoscale* **2018**, *10*, 4890; b) C. F. Du, Q. Liang, R. Dangol, J. Zhao, H. Ren, S. Madhavi, Q. Yan, *Nano-Micro Lett.* **2018**, *10*, 67; c) B. Song, K. Li, Y. Yin, T. Wu, L. Dang, M. Cabán-Acevedo, J. Han, T. Gao, X. Wang, Z. Zhang, J. R. Schmidt, P. Xu, S. Jin, *ACS Catal.* **2017**, *7*, 8549.

[10] a) Y. Jia, L. Zhang, G. Gao, H. Chen, B. Wang, J. Zhou, M. T. Soo, M. Hong, X. Yan, G. Qian, J. Zou, A. Du, X. Yao, *Adv. Mater.* **2017**, *29*, 1700017; b) Q. Xiong, Y. Wang, P. F. Liu, L. R. Zheng, G. Wang, H. G. Yang, P. K. Wong, H. Zhang, H. Zhao, *Adv. Mater.* **2018**, *30*, 1801450; c) Y. Yang, H. Fei, G. Ruan, J. M. Tour, *Adv. Mater.* **2015**, *27*, 3175; d) Y. Jiang, Y. Lu, J. Lin, X. Wang, Z. Shen, *Small Methods* **2018**, *2*, 1700369.

[11] a) J. Chang, Q. Lv, G. Li, J. Ge, C. Liu, W. Xing, *Appl. Catal., B* **2017**, *204*, 486; b) J. Chang, L. Liang, C. Li, M. Wang, J. Ge, C. Liu, W. Xing, *Green Chem.* **2016**, *18*, 2287.

[12] a) J. Chang, Y. Ouyang, J. Ge, J. Wang, C. Liu, W. Xing, *J. Mater. Chem. A* **2018**, *6*, 12353; b) J. Kibsgaard, T. F. Jaramillo, *Angew. Chem., Int. Ed.* **2014**, *53*, 14433.

[13] J. Chang, Y. Xiao, M. Xiao, J. Ge, C. Liu, W. Xing, *ACS Catal.* **2015**, *5*, 6874.

[14] a) P. Jiang, Q. Liu, Y. Liang, J. Tian, A. M. Asiri, X. Sun, *Angew. Chem., Int. Ed.* **2014**, *53*, 12855; b) Q. Liu, J. Tian, W. Cui, P. Jiang, N. Cheng, A. M. Asiri, X. Sun, *Angew. Chem., Int. Ed.* **2014**, *53*, 6710.

[15] M. C. Biesinger, B. P. Payne, A. P. Grosvenor, L. W. M. Lau, A. R. Gerson, R. S. C. Smart, *Appl. Surf. Sci.* **2011**, *257*, 2717.

[16] H. A. El-Sayed, A. Weiß, L. F. Olbrich, G. P. Putro, H. A. Gasteiger, *J. Electrochem. Soc.* **2019**, *166*, F458.

[17] K. Li, D. Rakov, W. Zhang, P. Xu, *Chem. Commun.* **2017**, *53*, 8199.

[18] Y. Huang, Y. Gao, Q. Zhang, Y. Zhang, J. J. Cao, W. Ho, S. C. Lee, *J. Hazard. Mater.* **2018**, *354*, 54.

[19] a) A. Dutta, A. K. Samantara, S. K. Dutta, B. K. Jena, N. Pradhan, *ACS Energy Lett.* **2016**, *1*, 169; b) S. Jin, *ACS Energy Lett.* **2017**, *2*, 1937; c) L.-A. Stern, L. Feng, F. Song, X. Hu, *Energy Environ. Sci.* **2015**, *8*, 2347.

[20] a) K. Zhu, W. Luo, G. Zhu, J. Wang, Y. Zhu, Z. Zou, W. Huang, *Chem. - Asian J.* **2017**, *12*, 2720; b) X. Wang, K. Du, Y. Y. Fredrik Liu, P. Hu, J. Zhang, Q. Zhang, M. H. S. Owen, X. Lu, C. K. Gan, P. Sengupta, C. Kloc, Q. Xiong, *2D Mater.* **2016**, *3*, 031009.

[21] H. A. Bandal, A. R. Jadhav, A. A. Chaugule, W. J. Chung, H. Kim, *Electrochim. Acta* **2016**, *222*, 1316.